Chapter 3

Enhancement of the catalytic activity of a homogeneous iron-based water oxidation catalyst through substrate effects of graphitic electrodes

*The synthesis, characterization and electrochemical studies of the dinuclear complex [(MeOH)Fe(Hbbpya)–μ-O–(Hbbpya)Fe(MeOH)](OTf)$_4$ (**1**) (with Hbbpya = N,N-bis(2,2'-bipyrid-6-yl)amine) are described. With the help of on-line electrochemical mass spectrometry, the complex is demonstrated to be active as a water oxidation catalyst. The complex shows a significantly lower catalytic overpotential on graphitic working electrodes compared to other electrode materials which is ascribed to specific interactions between the Hbbpya ligand in the complex and the surface of an sp^2 carbon electrode. Cyclic voltammetry experiments provide evidence that the structure of complex **1** undergoes reversible changes under high potential conditions, regenerating the original structure of complex **1** upon returning to lower potentials. Results from electrochemical quartz crystal microbalance experiments rule out that catalysis proceeds via deposition of catalytically active material on the electrode surface.*

The results presented in this chapter have been submitted for publication as a full paper: K.G. Kottrup, S. D'Agostini, P.H. van Langevelde, M.A. Siegler and D.G.H. Hetterscheid, *ACS Catal.* accepted for publication.

3.1 Introduction

An important aspect in homogeneous electrocatalysis which has so far received only little attention is the influence of the electrode surface on the reaction mechanisms involving homogeneous electrocatalysts. If the electron transfer between the catalyst and the electrode proceeds exclusively via an outer sphere mechanism, one would expect only a small influence of the electrode material. However, in case of an inner sphere mechanism involving adsorption of the catalyst on the electrode surface, a much larger influence of the electrode material is to be expected.[1] Despite the potentially very important role of the electrode material in electrochemical water oxidation catalysis only few examples of research on this subject can be found in literature.[2-3]

In this chapter we introduce the dinuclear oxo-bridged iron complex $[(MeOH)Fe(Hbbpya)–\mu\text{-}O–(Hbbpya)Fe(MeOH)](OTf)_4$ (**1**) (with Hbbpya = *N*,*N*-bis(2,2'-bipyrid-6-yl)amine). This complex was designed based on the results described in chapter 2. The Hbbpya ligand is free of β-hydrogen atoms which can lead to degradation of the ligand under strongly oxidizing conditions[4] and the aromatic structure of the Hbbpya ligand should provide additional stability towards oxidation compared to the aliphatic cyclam ligand. Furthermore, the Hbbpya ligand is expected to be more electron donating due to its more electron rich structure compared to cyclam. Finally, the amino group which bridges the two bipyridine moieties could provide a useful platform for additional ligand modifications in the future although such modifications have previously been reported to affect the structure of the resulting complex.[5]

To ensure that complex **1** can be studied with a variety of different electrode materials, halide ions are avoided to achieve compatibility of the complex with gold working electrodes.

The complex is active as an electrocatalyst for water oxidation, which is in line with previous reports that have found dinuclear oxygen-bridged iron complexes to be active water oxidation catalysts.[5-9] However, in case of complex **1** the results show that the water oxidation activity is strongly dependent on the nature of the electrode material, resulting in a significantly lower overpotential on graphitic working electrodes compared to other electrode materials.

3.2 Results and Discussion

3.2.1 Synthesis and Characterization

Complex **1** was synthesized by combining methanolic solutions of iron(II) triflate and Hbbpya under argon (Scheme 3.1). After stirring over night and subsequent evaporation of the solvent, a crude reddish/brownish solid was obtained. To isolate complex **1**, the crude product was recrystallized in air by vapor diffusion of Et_2O into a concentrated methanolic solution of the crude material, resulting in dark brown crystals of complex **1**. The crystalline material was characterized by single crystal X-ray crystallography, mass spectrometry and elemental analysis. X-ray structure determination unequivocally reveals the dimeric nature of complex **1** (Fig. 3.1). All relevant bond angles and distances of the crystal structure of **1** are summarized in table B.2 (Appendix B).

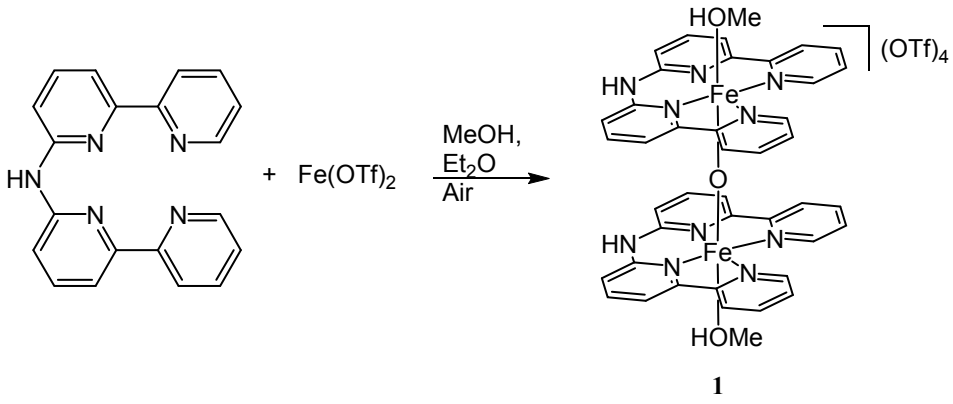

1

Scheme 3.1: Synthesis of complex **1**

The complex consists of two iron sites bridged by an oxo-ligand. Each iron site bears an Hbbpya ligand following a distorted square planar geometry and an axial methanol ligand. The measured bond angles and bond distances are very similar for both iron sites. All eight Fe–N bond distances fall into a narrow range of 2.11 to 2.14 Å. Both N–Fe–N bond angles of the six-membered chelate rings of 87.0° and 87.1° respectively are close to the ideal 90° of a square planar geometry. The N–Fe–N angles of the five-membered chelate rings are more acute at 78.2° to 78.7° while the open N–Fe–N bond angles are much wider at 114.2° and 114.6°. Both internal Fe–O bond distances between the iron centres and the bridging oxo-ligand of 1.78 Å are shorter than the external Fe–O bonds distances to the methanol ligands of 2.15 Å. These values are in good agreement with values

previously reported by Thummel et al. for the iron complexes [(H_2O)Fe(ppq)–μ-O–(ppq)FeCl]Cl_3 (**2**) (with ppq = 2-(pyrid-2'-yl)-8-(1",10"-phenanthrolin-2"-yl)-quinoline) and [Fe(dpa)Cl_2]Cl (**3**) (with dpa = *N*,*N*-di(1,10-phenanthrolin-2-yl)-*N*-isopentylamine).[5]

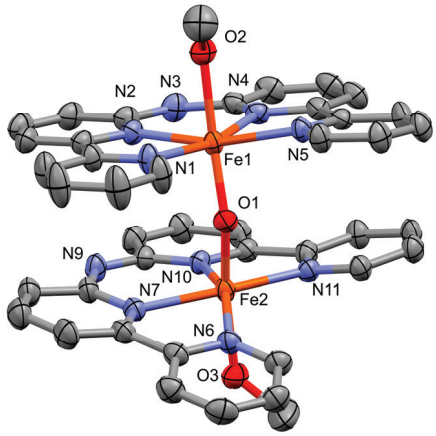

Figure 3.1: Displacement ellipsoid plot (50% probability level) of complex **1** at 110 K. All hydrogen atoms and the four triflate counter-ions have been omitted for clarity.

While the Fe–O–Fe bond angle in the structure of complex **2** was reported to be 171.3°, the Fe–O–Fe bond angle of 155.78° in complex **1** deviates notably from the expected 180°. The atoms of the two Hbbpya ligands are also not aligned directly on top of each other in the crystal structure. Instead each atom of the Hbbpya ligand bound to Fe1 is offset with respect to its counterpart in the Hbbpya ligand bound to Fe2 by a rotation around the Fe1-Fe2 axis of about 44° (Fig. B.1, Appendix B). Furthermore, the two Hbbpya ligands differ in their conformation. While one Hbbpya ligand is fairly planar with an internal torsion angle of only 3.0° (Fig. B.2, Appendix B), one of the two bipyridine moieties of the other Hbbpya ligand is twisted out of plane, resulting in a considerably greater internal torsion angle of 16.4° (Fig. B.2, Appendix B). As a result, the distances between the two Hbbpya ligands vary from a relatively narrow range of 3.37 Å to 3.55 Å for the two bipyridine moieties in face parallel alignment to a much wider spread of 3.52 Å to 4.40 Å for the other two bipyridine moieties (Fig. B.3, Appendix B). These features suggest that the distortions in the structure are compensated for by favourable π-π interactions between the aromatic systems of the two Hbbpya ligands. The observed distances of 3.37 Å to 3.55 Å fall well within the range commonly found for such interactions.[10]

Next to the structural data for the crystalline material, mass spectrometry data confirms that the complex exists exclusively as a dimeric species in aqueous solution (Fig. B.4, Appendix B). UV-vis measurements of the aqueous solution show no change in the absorption spectrum for at least 10 hours, confirming that the dimeric species is stable over time (Fig. B.5, Appendix B)

3.2.2 Electrochemical experiments

3.2.2a General considerations

Although complex **1** dissolves in water, it hardly dissolves in solutions containing perchlorate anions. As a consequence, sodium sulfate was chosen as the most appropriate electrolyte even though the sulfate ion has been shown to inhibit water oxidation activity slightly compared to perchlorate in some cases.[11] In 0.1 M Na_2SO_4 complex **1** does dissolve up to concentrations of 0.5 mM.

3.2.2b Electrochemistry on gold

Using a gold working electrode, the redox behavior of complex **1** was investigated by performing cyclic voltammetry (CV) experiments across different scan ranges. Figures 3.2a and 3.2b show the respective first and second scan of a CV experiment between 0.0 and 1.2 V vs. a reversible hydrogen electrode (RHE), starting each scan at 0.7 V vs. RHE. In the second scan (Fig. 3.2b), four distinct redox events can be observed, indicated as I, II, III and IV in the figure. I and IV are tentatively assigned to the $[Fe^{II}Fe^{II}]/[Fe^{II}Fe^{III}]$ transition and II and III to the $[Fe^{II}Fe^{III}]/[Fe^{III}Fe^{III}]$ transition. This assignment is supported by the fact that the oxidation event II at 0.9 V is largely absent in the first forward scan (Fig. 3.2a) as long as a starting potential above both reduction events III and IV is chosen. Since the complex is introduced in the $[Fe^{III}Fe^{III}]$ state and the selected resting potential of 0.7 V lies above both reduction events, hardly any $[Fe^{II}Fe^{III}]$ is present to be oxidized in the first scan. Further evidence for this assignment is obtained when the starting potential is set to 0.2 V and the scan range is selected to stay below the onset of second oxidation event between 0.8 and 1.0 V. The corresponding voltammogram between 0.2 and 0.8 V (Fig. 3.2c) only shows transitions I and IV, showing that reduction wave IV is connected to oxidation wave I, and that reduction wave III is connected to oxidation wave II.

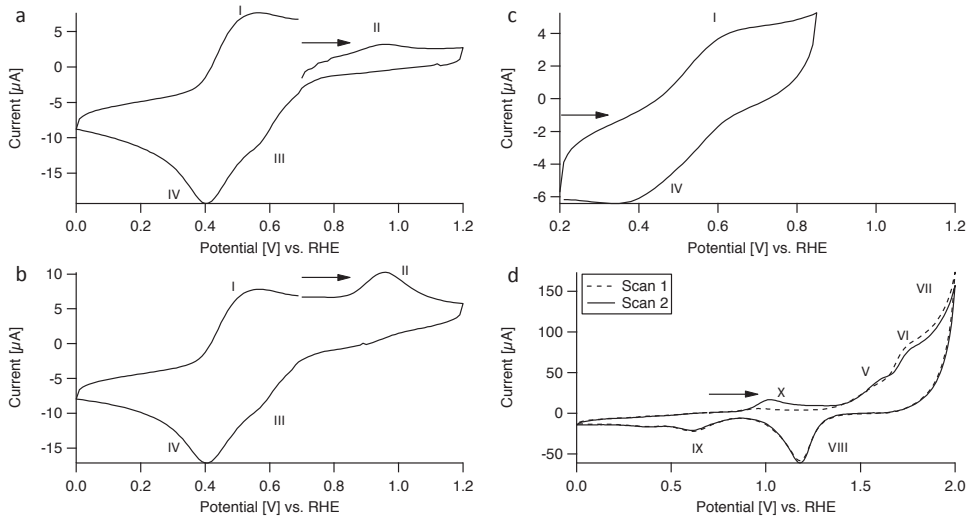

Figure 3.2: Results of CV experiments of 0.5 mM complex **1** in a 0.1 M Na_2SO_4 solution using a gold working electrode scanning at 100 mV/s. Arrows indicate the direction of each cycle. (a) First scan between 0.0 and 1.2 V vs. RHE, starting at 0.7 V vs. RHE. (b) Second scan between 0.0 and 1.2 V vs. RHE, starting at 0.7 V vs. RHE. (c) Second scan between 0.2 and 0.8 V vs. RHE, starting at 0.2 V vs. RHE. (d) First and second scan between 0.0 and 2.0 V vs. RHE, starting at 0.7 V vs. RHE.

When the scan range is set to 0.0-2.0 V, a shift in the redox behavior is observed. Starting again at 0.7 V, the first forward does not show any new oxidation events below 1.5 V (Fig. 3.2d). Above 1.5 V three oxidation events are observed, labeled V, VI and VII, which can be attributed to gold oxide formation (V and VI) and water oxidation (VII) respectively (vide infra).

In the backward scan, two reduction events can be seen, one at 1.2 V (VIII; gold oxide reduction) and one at 0.6 V (IX). In the second forward scan, one additional oxidation event (X) appears at 1.0 V. Instead of the four transitions I, II, III and IV that were initially observed for the Fe^{II}/Fe^{III} redox events when scanning between 0.0 and 1.2 V, only the two new and broad redox events IX and X can be observed below 1.2 V in subsequent cycles after reaching 2.0 V. This difference indicates that complex **1** undergoes structural changes at high potentials. Scanning from 0.0 to 2.0 V and recording 50 scans between 0.0 and 1.2 V at 100 mV/s immediately afterwards shows that this change in redox behavior reverts over time; waves IX and X disappear while the waves I-IV reappear during prolonged scanning, showing that the change to the structure of complex **1** is reversible (Fig. 3.3).

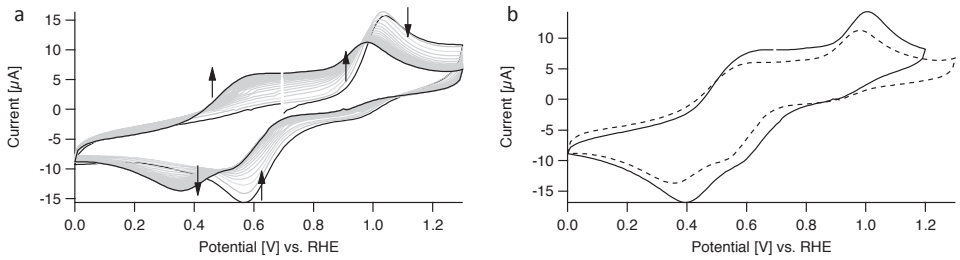

Figure 3.3: Demonstration of the evolution over time of the redox events observed after initially scanning to 2.0 V vs. RHE with a gold working electrode in the presence of 0.5 mM complex **1**. The change in time is visualized with CV experiments between 0.0 and 1.3 V vs. RHE at a scan rate of 100 mV/s. All experiments were performed in a 0.1 M Na_2SO_4 solution. (a) 50 cycles between 0.0 and 1.3 V vs. RHE, starting at 0.7 V vs. RHE, recorded immediately after scanning to 2.0 V vs. RHE. The first and the last scan are displayed in black while the intermediate scans are displayed in grey. Arrows indicate the change in the current profile over time. (b) Comparison between the redox events before scanning to 2.0 V vs. RHE (solid line) and scan number 50 after scanning to 2.0 V vs. RHE (dashed line).

Evidence that the irreversible oxidation wave VII belongs to the oxygen evolution reaction was obtained via OLEMS experiments. In OLEMS experiments the *m/z* traces of selected gaseous species sampled in solution in close proximity to the surface of the working electrode are recorded during electrochemical experiments.[12] Figure 3.4 shows the second forward scan of an OLEMS experiment, recorded while cycling the potential between 1.3 and 2.0 V at 1 mV/s, with a starting potential of 1.3 V. The bottom panel of figure 3.4 shows the corresponding current trace. Since the gold electrode was already oxidized during the first scan of the OLEMS experiment, the gold oxidation waves V and VI are absent in the second scan, leaving only the oxidation wave VII. The top panel of figure 3.4 shows the mass trace for O_2 recorded during the experiment which shows a clear onset of oxygen evolution at about 1.9 V that correlates well with the oxidative current shown in the bottom panel of figure 3.4. Since previous reports[13-15] have shown that electrocatalytic water oxidation by metal complexes is often preceded or accompanied by oxidative degradation of ligands, which can result in the formation of CO_2, we also recorded the mass trace of CO_2 via OLEMS (Fig. 3.4, middle). The result shows that, compared to oxygen, no significant amounts of CO_2 are being formed during the experiment.

The gold electrode in itself is in principle capable of oxidizing water at high potentials, however, in previous work no detectable amounts of oxygen were found below 2.0 V for a gold working electrode in the absence of any additional catalyst.[16] While there is still some oxidative current beyond gold oxidation that is visible in blank measurements, OLEMS measurements with a gold working

electrode in a 0.1 M Na_2SO_4 electrolyte solution in the absence of complex **1** confirm that there is no detectable amount of oxygen being formed below 2.0 V under those conditions (Fig. B.6, Appendix B).

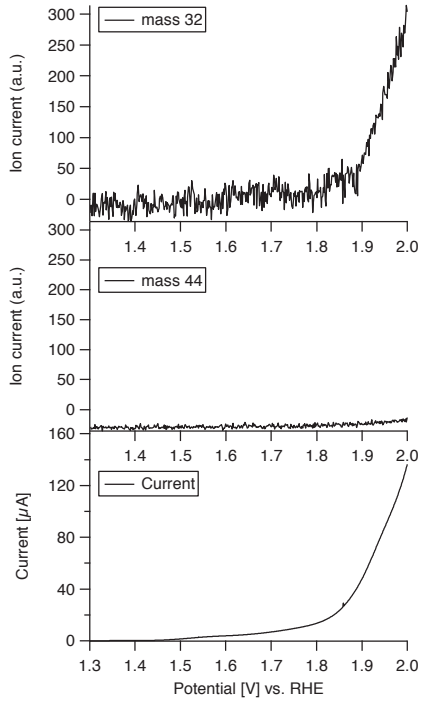

Figure 3.4: Results of an OLEMS measurement of 0.5 mM complex **1** with a gold working electrode in a 0.1 M Na_2SO_4 solution (scan range, 1.3-2.0V vs. RHE, scan rate 1 mV/s, starting at 1.3 V vs. RHE). Shown is the forward scan of a CV experiment with the *m/z* trace for O_2 (top), the *m/z* trace for CO_2 (middle) and the corresponding current (bottom).

3.2.2c Electrochemistry on carbon

The electrochemistry that is observed for complex **1** with a pyrolytic graphite (PG) working electrode shows a significant difference from the results obtained for a gold working electrode. For both electrodes, complex **1** initially shows redox waves I-IV (Fig. 3.5a) which disappear when the potential is increased to 2.0 V, resulting in the formation of a new species, giving rise to redox waves IX and X (Fig. 3.5b). Likewise, for both electrode materials the disappearance of waves IX and X accompanied by the reappearance of waves I-IV can be seen over time when the potential is kept below 1.2 V after initially scanning to 2.0 V (Fig. 3.5c-d). However, in contrast to the electrochemistry on gold, an additional and persistent irreversible oxidation wave can be observed on PG with an onset potential of about 1.6 V (Fig. 3.6, bottom).

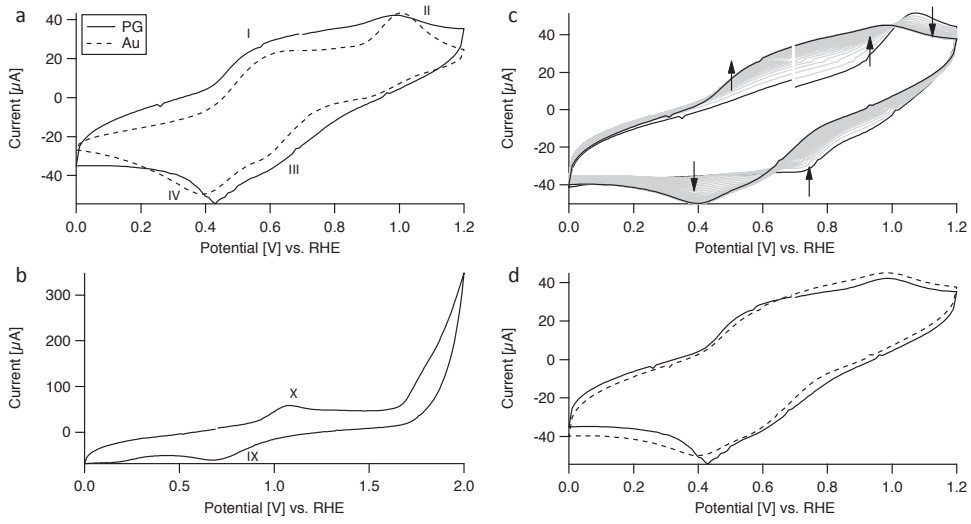

Figure 3.5: Shown are several voltammograms of 0.5 mM complex **1** in a 0.1 M Na_2SO_4, recorded at 100 mV/s, each with a starting potential of 0.7 V vs. RHE. (a) Results of scanning between 0.0 and 1.2 V vs. RHE on a PG working electrode and a gold working electrode. The current recorded for the gold working electrode was normalized by a factor of 3 for the sake of comparison. Shown is the second scan of each experiment. (b) Results of scanning between 0.0 and 2.0 V vs. RHE on a PG working electrode. (c) 50 cycles between 0.0 and 1.3 V vs. RHE, recorded on a PG working electrode immediately after scanning to 2.0 V vs. RHE. The first and the last scan are displayed in black while the intermediate scans are displayed in grey. Arrows indicate the change in the current profile over time. (d) Comparison between the redox events recorded on a PG working electrode before scanning to 2.0 V vs. RHE (solid line) and scan number 50 after scanning to 2.0 V vs. RHE (dashed line).

While the separation between the two waves above 1.6 V is not very well resolved at higher scan rates (100 mV/s, Fig. 3.5b), it becomes much more pronounced at lower scan rates (10 mV/s and slower, Fig. 3.6, bottom and Fig. 3.7b).

OLEMS measurements for complex **1** with PG were performed under the same conditions as the respective experiments with gold, recording the mass traces for O_2 and CO_2 while cycling the potential between 1.3 and 2.0 V at 1 mV/s with a starting potential of 1.3 V. The recorded current (Fig. 3.6, bottom) shows two oxidation events in the forward scan from around 1.6 V onward. The corresponding O_2 trace (Fig. 3.6, top) shows that oxygen evolution follows the recorded current profile which suggests that both oxidation waves correspond to an oxygen evolution reaction. It appears that the formation of dioxygen is feasible for complex **1** in combination with a PG working electrode starting around 1.6 V whereas with a gold working electrode this is not the case until about 1.9 V. (compare Fig. 3.6, top and bottom with Fig. 3.4, top and bottom).

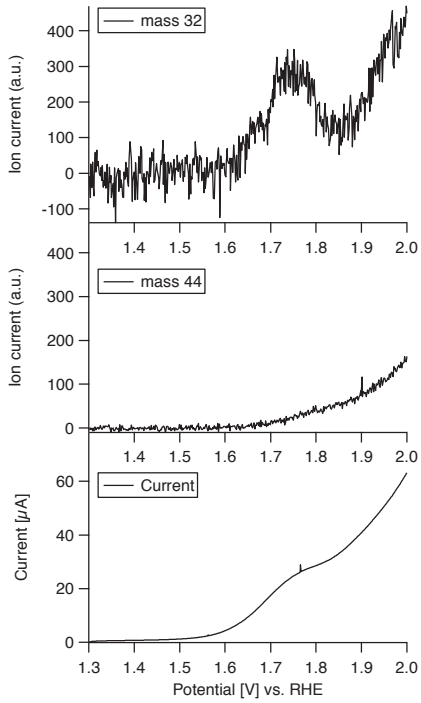

Figure 3.6: Results of an OLEMS measurement for 0.5 mM complex **1** on a PG working electrode in a 0.1 M Na_2SO_4 solution (scan range, 1.3-2.0V vs. RHE, scan rate 1 mV/s, starting at 1.3 V vs. RHE). Shown is the forward scan of a CV experiment with the *m/z* trace for O_2 (top), *m/z* trace for CO_2 (middle) and the corresponding current (bottom).

Aside from oxygen evolution, significant amounts of CO_2 are produced simultaneously at oxidative potentials when a PG working electrode is used (Fig. 3.6, middle). While it is difficult to unambiguously assign either the complex or the electrode material as the source of the CO_2, the results obtained when using a gold working electrode suggest that most of the CO_2 does indeed originate from the oxidation of pyrolytic graphite. This hypothesis is supported by the observation that for a solution containing $Fe(OTf)_2$ instead of complex **1**, CO_2 formation of the same order of magnitude with roughly the same onset potential is observed (vide infra).

In contrast to gold, a PG working electrode does not produce any detectable amounts of oxygen in the absence of an additional catalyst even at potentials significantly greater than 2.0 V (cf. chapter 5, Fig. 5.2). This shows clearly that the presence of complex **1** is crucial for the formation of dioxygen observed during the experiment.

The apparent difference in reactivity of complex **1** between experiments with a gold working electrode and a PG working electrode prompted us to look further

into the correlation between the properties of the electrode surface and the resulting electrochemistry. Using a glassy carbon (GC) working electrode in combination with complex **1** yields results that are qualitatively identical to those obtained on PG, both with respect to the redox behavior (Fig. 3.7a-b) and the two oxidation waves above 1.6 V (Fig. 3.7b). Voltammograms recorded with a boron doped diamond (BDD) working electrode instead only show a single oxidation event above 1.6 V (Fig. B.7, Appendix B), similar to the results for a gold working electrode, instead of the two distinct waves observed for graphitic electrode materials. The comparison between the results obtained for the four different electrode materials points to different modes of activity for complex **1** on graphitic working electrodes compared to non-graphitic working electrodes.

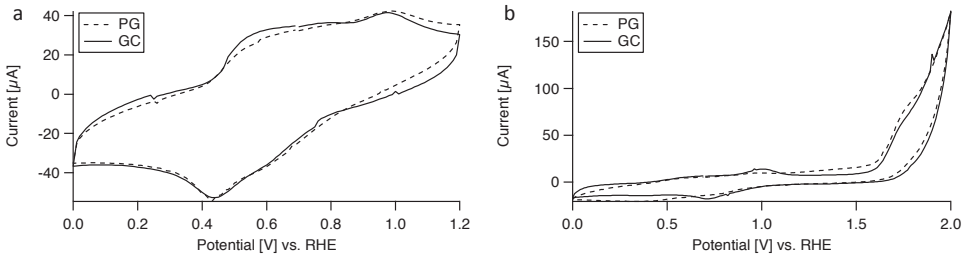

Figure 3.7: Shown are voltammograms of 0.5 mM complex **1** in a 0.1 M Na_2SO_4 solution recorded on different working electrodes. (a) Comparison of the results using a PG and a GC working electrode. Shown is the respective second scan of each experiment, recorded between 0.0 and 1.2 V vs. RHE at 100 mV/s with a starting potential of 0.7 V vs. RHE. The current recorded on GC was normalized by a factor of 4.5 for the sake of comparison. (b) Comparison of the results using a PG and a GC working electrode. Shown is the respective second scan of each experiment, recorded between 0.0 and 2.0 V vs. RHE at 10 mV/s with a starting potential of 0.7 V vs. RHE. The current recorded on GC was normalized by a factor of 4.5 for the sake of comparison.

3.2.3 Homogeneous catalyst vs. heterogeneous surface deposit

Since Fe_2O_3 is known to be a catalyst for water oxidation,[17-20] it is important to establish that no such deposits are being formed on the working electrode, which then may be responsible for (part of) the observed reactivity. To rule out the formation of catalytically active surface deposits, electrochemical quartz crystal microbalance (EQCM) experiments were carried out with a gold working electrode.[21-22] The working electrode in EQCM experiments consists of a thin layer of gold, deposited on a quartz crystal oscillator. Mass changes at the working electrode can be detected by measuring changes in the resonance frequency of the quartz crystal. To avoid damaging the thin gold layer of the EQCM electrode and due to the mass change associated with gold oxide formation and reduction,

the potential was kept above 1.3 V at all times during EQCM experiments to avoid gold oxide reduction. The results show no significant change in the mass of the electrode for the potential window between 1.3 and 2.0 V at 1 mV/s in the presence of complex **1** (Fig. 3.8a).

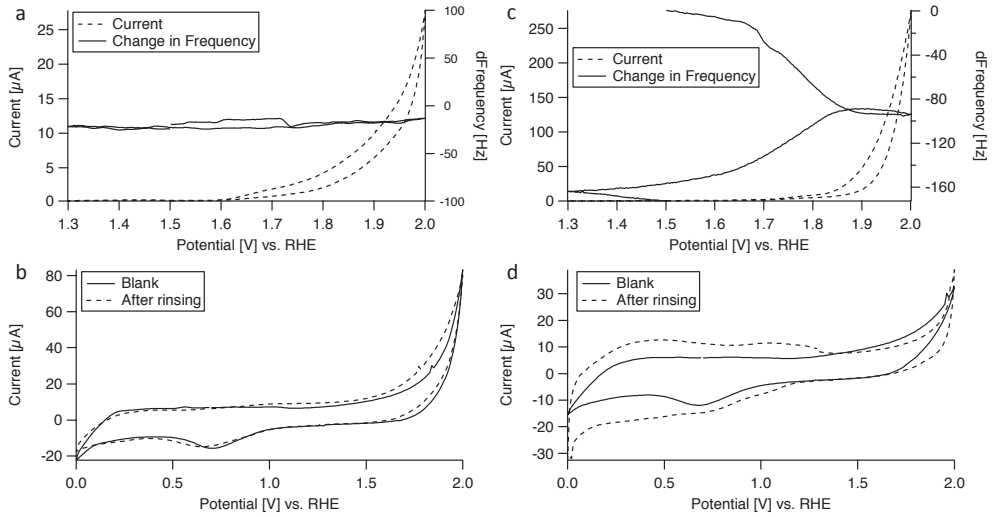

Figure 3.8: (a) Results of an EQCM experiment of 0.5 mM complex **1** in a 0.1 M Na_2SO_4 solution, recorded between 1.3 and 2.0 V vs. RHE with a gold working electrode at 1 mV/s, starting at 1.5 V vs. RHE. (b) Voltammograms of a freshly polished PG working electrode in a blank solution of 0.1 M Na_2SO_4 and the same PG working electrode in a blank 0.1 M Na_2SO_4 solution after cycling 3 times between 1.3 and 2.0 V vs. RHE at 1 mV/s in the presence of 0.5 mM complex **1** in a 0.1 M Na_2SO_4 solution and subsequent rinsing in the electrode. Both voltammograms were recorded between 0.0 and 2.0 V vs. RHE at 10 mV/s, starting at 0.7 V vs. RHE. (c) Result of an EQCM experiment of 1 mM $Fe(OTf)_2$ in a 0.1 M Na_2SO_4, recorded between 1.3 and 2.0 V vs. RHE with a gold working electrode at 1 mV/s, starting at 1.5 V vs. RHE. (d) Voltammograms of a freshly polished PG working electrode in a blank solution of 0.1 M Na_2SO_4 and the same PG working electrode in a blank 0.1 M Na_2SO_4 solution after cycling 3 times between 1.3 and 2.0 V vs. RHE at 1 mV/s in the presence of 1 mM $Fe(OTf)_2$ in a 0.1 M Na_2SO_4 solution and subsequent rinsing in the electrode. Both voltammograms were recorded between 0.0 and 2.0 V vs. RHE at 10 mV/s, starting at 0.7 V vs. RHE.

Since no graphitic EQCM electrodes were available, a PG working electrode was instead cycled 3 times between 1.3 and 2.0 V at a scan rate of 1 mV/s in the presence of complex **1**, taken out of the electrolyte solution and rinsed. A subsequently recorded voltammogram measured in a 0.1 M Na_2SO_4 electrolyte solution in the absence of complex **1** showed no additional current above the background of a blank measurement (Fig. 3.8b). These results show that if any electrode deposition does occur during catalytic water oxidation mediated by complex **1** it must be a highly reversible process.

In contrast to the results obtained for complex **1**, EQCM experiments in the presence of 1 mM $Fe(OTf)_2$ show a clear change in the mass of the gold electrode under identical conditions, indicating the formation of a deposit on the electrode surface (Fig. 3.8c). Similarly, cycling a PG working electrode 3 times between 1.3 and 2.0 V at 1 mV/s in the presence of $Fe(OTf)_2$ with subsequent rinsing of the electrode and recording a CV measurement between 0.0 and 2.0 V in a 0.1 M Na_2SO_4 electrolyte solution without $Fe(OTf)_2$ present yields a voltammogram which is different from that of a blank measurement (Fig. 3.8d). OLEMS measurements of $Fe(OTf)_2$ on a PG working electrode reveal water oxidation activity, albeit with a different current profile and higher onset potential for the oxygen evolution reaction compared to complex **1** (Fig. B.8, Appendix B).
The ion current for CO_2 measured with a PG working electrode in the presence of complex **1** and $Fe(OTf)_2$ respectively is of the same order of magnitude (compare Fig. 3.6, middle with Fig. B.8, middle, Appendix B) despite $Fe(OTf)_2$ lacking any ligand that could conceivably be oxidized to CO_2 under these conditions, providing further evidence for the assumption that the CO_2 formation observed in OLEMS experiments with complex **1** on a PG working electrode originates predominantly from the oxidation of the electrode material rather than oxidation of the ligand.

3.2.4 Mechanistic considerations

For PG, GC and Au working electrodes, we found that the redox behavior of complex **1** in solution changes upon exposure to high potentials. When kept at lower potentials afterwards, it slowly reverts to the original behavior (Fig. 3.3 and Fig 3.5c-d). Since mass spectrometry and UV-vis spectroscopy show that complex **1** exists exclusively as a dimer at the start of the experiment, this reversibility means that the dimeric structure is regenerated at lower potentials. A possible explanation could be that the complex falls apart into two Fe(Hbbpya) monomers upon oxidation to the Fe^{IV} or Fe^{V} state which re-associate to form complex **1** in the Fe^{III} state.
Evidence for the molecular nature of the catalytically active species was obtained from EQCM experiments on gold in which no mass changes of the electrode were observed in the presence of complex **1** under catalytic conditions. From control experiments with $Fe(OTf)_2$ instead of complex **1** we can rule out any potential pathways involving de-coordination of the Hbbpya ligand leading to the subsequent formation of the active catalyst in the form of solid deposits on the electrode surface.

For the combination of complex **1** with graphitic working electrodes, oxygen evolution was observed already at significantly lower potentials compared to complex **1** in combination with other electrode materials. This suggests that the first oxidation wave above 1.6 V seen on both PG and GC (Fig. 3.7b) might be related to specific interactions between the catalyst and a graphitic electrode surface. The difference in oxygen evolution activity of complex **1** on a graphitic working electrode compared to a gold working electrode strongly suggests a mechanism other than the involvement of surface oxides which has previously been suggested for a flavin-based water oxidation catalyst.[2] Instead, hydrophobic interactions for example in the form of π-π stacking between the aromatic Hbbpya ligand and an sp^2 carbon surface might take place.[23-28] The substrate influence of graphitic electrodes has an apparent beneficial influence on the water oxidation capabilities of complex **1**, leading to a significantly earlier onset of oxygen evolution on PG and GC working electrodes compared to BDD and gold working electrodes.

When comparing the voltammogram recorded for a PG working electrode in a blank 0.1 M Na_2SO_4 solution before and after being cycled 3 times between 1.3 and 2.0 V at 1 mV/s in the presence of complex **1**, we found no difference in the recorded current. This means that the interaction between complex **1** and the surface of a graphitic electrode must be highly reversible in nature and does not lead to the formation of a lasting adsorbed state.

3.2.5 Kinetic considerations

To compare the catalytic activity of complex **1** between a gold working electrode and a graphitic working electrode and also to compare the catalytic activity of complex **1** with other catalysts reported in literature, it is important to know the rate at which catalysis occurs. We used equation 1 to determine the TOF of complex **1** at different overpotentials.[29] In this equation, ν is the scan rate of the experiment, i_p is the current of oxidation wave X (cf. Fig. 3.2 and Fig. 3.5) while i_{cat} is the catalytic current at the potential for which the TOF is to be determined. Additional details about the calculations are available in appendix B.

$$TOF = 0.4848 \cdot \nu \left(\frac{i_{cat}}{i_p}\right)^2 \quad (1)$$

For the case of complex **1** with a PG working electrode we calculated the TOF at 1.75 V. For the comparison with gold we calculated the TOF of complex **1** with a gold working electrode at 1.9 and 2.0 V respectively. We refrained from calculating a TOF for complex **1** with a PG electrode at potentials higher than 1.75 V since the rate of CO_2 formation becomes non-negligible as is evident from the OLEMS measurement (Fig. 3.6). For the case of a PG working electrode a TOF of 0.4 s^{-1} was found for complex **1** at 1.75 V while for the case of a gold working electrode, TOFs of 0.4 and 1.4 s^{-1} were found for complex **1** at 1.9 and 2.0 V respectively. The comparison shows that complex **1** reaches the same TOF at 150 mV less overpotential with a PG working electrode compared to a gold working electrode.

Comparison of the catalytic performance with data from literature is complicated by the fact that the majority of kinetic studies has been carried out in the presence of chemical oxidants rather than electrochemically which leads to a poorly defined overpotential for those cases.

However, the rate determined for complex **1** with graphitic working electrodes compare favourably to values reported in literature despite the comparatively modest overpotential of 520 mV (1.75 V vs. RHE) as most iron-based catalysts have been reported to exhibit TOFs of the order of 0.1 s^{-1} or lower in water. Typical examples range from 0.012 s^{-1} reported by Akermark et al. to 0.23 s^{-1} for the Fe(bpmcn) system reported by Costas et al.[30-31] Some notable exceptions are the Fe(TAML) catalysts by Collins et al. and the Fe(ppq) catalyst by Thummel et al. for which initial rates of 1.3 s^{-1} and 2.2 s^{-1} respectively were found in the presence of excess CAN.[5, 32]

3.3 Conclusions

Complex **1** was found to be active as an electrocatalyst for the water oxidation reaction. Results obtained from EQCM experiments rule out the possibility of the formation of a solid deposit on the electrode surface as the true catalytic species, highlighting the stability of complex **1** under catalytic conditions and providing evidence for the molecular nature of the catalytically active species.

The results of CV experiments show a clear shift in the observed Fe^{II}/Fe^{III} redox behaviour after exposure of complex **1** to high potentials (2.0 V vs. RHE) which suggests that complex **1** is merely the pre-catalyst and not the true active species. However, in a subsequent CV experiment the original redox behaviour of complex

1 was recovered over time, showing that the change in redox behaviour is reversible and that the dimeric structure of complex **1** is regenerated.
Compared to other iron-based water oxidation electrocatalysts, complex **1** exhibits a remarkably low onset potential of oxygen evolution in combination with a PG working electrode with a recorded overpotential on the scale of only 300-400 mV with respect to the thermodynamic potential of the water oxidation reaction of 1.23 V. Based on a comparison of the catalytic behavior of complex **1** with working electrodes made up of different materials, the onset potential of oxygen evolution observed in the case of graphitic working electrodes is significantly lower compared to experiments with a gold working electrode, demonstrating a strong substrate influence of the electrode material on the catalytic performance.

Additionally, our analysis of the kinetics of the catalytic reaction suggest that complex **1** performs better in combination with a graphitic working electrode compared to a gold working electrode as 150 mV more overpotential are required to achieve the same turnover frequency for complex **1** in case of a gold working electrode compared to a PG working electrode. This means that for any attempts to benchmark water oxidation catalysts electrochemically a possible influence of the electrode material must be considered.
To the best of our knowledge, our findings represent the first evidence that substrate effects of the electrode material can lead to a significant reduction of the overpotential of a homogeneous electrocatalyst for the water oxidation reaction, emphasizing the importance of the electrode material in electrocatalytic applications.

3.4 Experimental

3.4.1 General

tert-Butylamine was purchased from Acros Organics. 2,2'-Bipyridine, *m*CPBA, 6-bromo-2,2'-bipyridine, (S)-BINAP, iron powder, $PhCF_3$ and KO*t*Bu were purchased from Sigma Aldrich. *p*-Toluensulfonic acid anhydride was purchased from VWR. $Pd(dba)_2$, TFA and MTBE were purchased from Fisher Scientific. All chemicals were used as received and without further purification. The concentration of *m*CPBA was determined via titration with sodium thiosulfate before use. (S)-BINAP, iron powder, $PhCF_3$ and KO*t*Bu were stored under argon.

2,2'-Bipyridine mono N-oxide, 6-amino-2,2'-bipyridine and *N*,*N*-bis(2,2'-bipyrid-6-yl)amine were synthesized according to literature procedures.[33-35] Solvents were degassed according to standard freeze-pump-thaw protocols.
UV-vis spectra were recorded on a Varian Cary 50 Scan spectrophotometer. Mass spectra were measured on a Thermo Scientific MSQ Plus ESI spectrometer. Elemental analyses were performed by Mikroanalytisches Laboratorium Kolbe in Germany.

3.4.2 Electrochemical experiments

All electrochemical measurements with the exception of the EQCM experiments (details below) were performed in custom made single-compartment glass cells, recorded on Ivium potentiostats, operated by IviumSoft software, using a three electrode setup with the working electrode in hanging meniscus configuration. The working electrodes used in the experiments were a pyrolytic graphite (PG) disc, two gold disc electrodes of different sizes, a glassy carbon (GC) rod and a boron doped diamond (BDD) disc. The respective (geometric) surface areas are 0.2 cm^2 (PG), 0.13 cm^2 and 0.5 cm^2 (gold), and 0.07 cm^2 (GC and BDD). A large surface area gold plate was used as a counter electrode in all experiments. The reference electrode was a reversible hydrogen electrode (RHE) made up of a platinum mesh in H_2-saturated electrolyte at the same pH as the electrolyte solution inside the cell. The cell and the reference electrode were connected via a Luggin capillary.
The PG electrode was prepared before each experiment by polishing the electrode surface with sandpaper. The GC electrode was prepared by polishing the electrode surface with sandpaper first and subsequently with alumina suspensions (1.0 micron followed by 0.3 micron). For both the PG and the GC electrodes, the polishing was followed by removal of excess debris by sonicating the electrode in Milli-Q water for at least 5 minutes.
The gold electrodes were prepared before each experiment by oxidizing the surface at 10 V for 30 s in a 10% H_2SO_4 solution, followed by stripping of the gold oxide layer in a 6 M HCl solution and subsequent electro-polishing of the electrode by scanning for 200 cycles between 0.0 and 1.75 V vs. RHE at 1000 mV/s in a 0.1 M $HClO_4$ electrolyte solution.
The BDD electrode was prepared before each experiment by sonication for 5 minutes in concentrated HNO_3 followed by sonication for 5 minutes in Milli-Q water.

All glassware used in electrochemical measurements was routinely cleaned of any organic contamination by boiling in a 3:1 mixture of concentrated sulfuric and nitric acid. Prior to each experiment, the glassware was cleaned by threefold rinsing and boiling in Milli-Q water. All electrolyte solutions were prepared from p.a. grade chemicals (Merck Suprapur®) and Milli-Q water (resistivity > 18.2 MΩ). Prior to measurements, the electrolyte solution was purged of air by bubbling with argon (Linde, Ar 6.0) for at least 20 minutes. During the measurements, the cell was constantly kept under argon flow to prevent air from entering.

For the OLEMS measurements, the gasses formed at the working electrode were collected via a hydrophobic tip (KEL-F with a porous Teflon plug) in close proximity to the surface of the working electrode and analyzed in a QMS 200 mass spectrometer. A detailed description of the OLEMS setup is available elsewhere.[12] For the mass spectrometry data recorded during cyclic voltammetry experiments, background correction was done by assuming an exponential decay fit (concerns figures 3.4, 3.6, B.6 and B.8).

EQCM experiments were performed in a 3 mL Teflon cell purchased from Autolab. The top part of the cell was modified to allow for electrochemical measurements under an inert atmosphere. For further details, see figure B.9, Appendix B. The EQCM was controlled by an Autolab potentiostat operated by NOVA 2.0 software. Autolab EQCM electrodes with a surface area of 1.5 cm^2 consisting of a 200 nm gold layer deposited on a quartz crystal were used as working electrodes. A custom made RHE reference electrode was used which is described elsewhere.[13]

3.4.3 Synthesis of $Fe(OTf)_2 \cdot 5.5H_2O$

Iron powder (1.44 g, 25.8 mmol) was carefully added in portions to 4.5 mL 98% triflic acid (50.0 mmol) in 30 mL water at room temperature while stirring. After all gas evolution ceased, the mixture was heated to 60°C for 1 h while maintaining stirring. The remaining solids were removed by filtration and the water was evaporated under vacuum, yielding a white powder with a slight blue/green hue which was dried under vacuum. Yield: 8.6 g (19.0 mmol, 76%)

The dried product was stored under argon to prevent subsequent changes in the hydration state over time.

Elemental analysis calcd. (%) for $C_2F_6Fe_2O_6S_2 \cdot 5.5H_2O$ (453.0 g/mol): C 5.30, H 2.45, N 0.00 Found: C 5.28, H 2.46, N 0.00.

*3.4.4 Synthesis of [(MeOH)Fe(Hbbpya)–μ-O–(Hbbpya)Fe(MeOH)](OTf)$_4$ (**1**)*

N,*N*-bis(2,2'-bipyrid-6-yl)amine (24 mg, 0.07 mmol) was dissolved in 2 mL degassed methanol. Subsequently $Fe(OTf)_2 \cdot 5.5H_2O$ (34 mg, 0.07 mmol) dissolved in 2 mL degassed methanol was added, resulting in a deep red solution. The mixture was left to stir over night under N_2 atmosphere at room temperature. After removal of the solvent in vacuum, the obtained crude product was dissolved in a small amount of methanol (~1 mL). Complex **1** was obtained as dark brown crystals through slow vapor diffusion of diethyl ether into the methanolic solution of the crude product in air. The crystals were collected by filtration, washed with diethyl ether followed by washing with a small amount of cold methanol and subsequently dried in air. Yield: 39 mg (0.03 mmol, 73%)

ESI-MS (H_2O): Found: $[Fe^{III}(bbpya)–\mu\text{-}O–(bbpya)Fe^{III}]^{2+}$ m/z = 388.6; calcd.: m/z = 388.1

Elemental analysis calcd. (%) for $C_{46}H_{38}F_{12}Fe_2N_{10}O_{15}S_4 \cdot 2H_2O$ (1474.0 g/mol): C 37.46, H 2.87, N 9.50; Found: C 37.61, H 2.91, N 9.63.

3.4.5 Sample preparation

Due to slow dissolution of complex **1** in 0.1 M Na_2SO_4 electrolyte solution, the complex was initially dissolved in a small amount of Milli-Q water (typically 1-2 mL) and subsequently added to the electrochemical cell containing the electrolyte solution. The concentration of electrolyte in the cell was adjusted to account for the resulting dilution.

For electrochemical experiments with complex **1**, the complex was dissolved in air-saturated Milli-Q water and subsequently added to the electrochemical cell after complete dissolution. The electrolyte was then purged of air again by bubbling with argon for several minutes. To achieve faster dissolution of complex **1** in water, the crystals were powderized before dissolving them in water.

For electrochemical experiments with $Fe(OTf)_2$, the salt was dissolved in a small amount of electrolyte taken from the electrochemical cell and subsequently added again to the electrochemical cell after complete dissolution. The electrolyte was then purged of air again by bubbling with argon for several minutes.

All experiments in this report were performed at concentrations of 0.5 mM for complex **1** and 1 mM for $Fe(OTf)_2$ unless otherwise specified.

3.5 Supporting Info

The following supplementary information can be found in Appendix B: Details about the structural features in the crystal structure of complex (Fig. B.1-B.3), mass spectrometric data for complex **1** in water (Fig. B.4), UV-vis spectra of complex **1** in aqueous solution (Fig. B.5), results of an OLEMS blank experiment with a gold working electrode (Fig. B.6), a voltammogram of complex **1** recorded with a BDD working electrode (Fig. B.7), results of an OLEMS experiment of $Fe(OTf)_2$ with a PG working electrode (Fig. B.8), a depiction of the modified cell used in EQCM experiments (Fig. B.9), details about the calculation of turnover frequencies of complex **1** with gold and PG working electrodes as well as crystallographic data of complex **1**.

3.6 References

[1] A. J. Bard; L. R. Faulkner, In *Electrochemical methods: fundamentals and applications*, 2nd ed.; Wiley: 2001; pp 115-117.
[2] E. Mirzakulova; R. Khatmullin; J. Walpita; T. Corrigan; N. M. Vargas-Barbosa; S. Vyas; S. Oottikkal; S. F. Manzer; C. M. Hadad; K. D. Glusac, *Nat. Chem.* **2012**, *4*, 794-801.
[3] S. W. Sheehan; J. M. Thomsen; U. Hintermair; R. H. Crabtree; G. W. Brudvig; C. A. Schmuttenmaer, *Nat. Commun.* **2015**, *6*, 6469.
[4] T. J. Collins, *Acc. Chem. Res.* **1994**, *27*, 279-285.
[5] L. D. Wickramasinghe; R. Zhou; R. Zong; P. Vo; K. J. Gagnon; R. P. Thummel, *J. Am. Chem. Soc.* **2015**, *137*, 13260-13263.
[6] M. M. Najafpour; A. N. Moghaddam; D. J. Sedigh; M. Hołyńska, *Catal. Sci. Technol.* **2014**, *4*, 30-33.
[7] B. Zhang; F. Li; F. Yu; H. Cui; X. Zhou; H. Li; Y. Wang; L. Sun, *Chem. - Asian J.* **2014**, *9*, 1515-1518.
[8] D. Wang; L. Que, Jr., *Chem. Commun.* **2013**, *49*, 10682-10684.
[9] A. R. Parent; T. Nakazono; S. Lin; S. Utsunomiya; K. Sakai, *Dalton Trans.* **2014**, *43*, 12501-12513.
[10] C. R. Martinez; B. L. Iverson, *Chem. Sci.* **2012**, *3*, 2191-2201.
[11] O. Diaz-Morales; T. J. Hersbach; D. G. H. Hetterscheid; J. N. Reek; M. T. M. Koper, *J. Am. Chem. Soc.* **2014**, *136*, 10432-10439.
[12] A. H. Wonders; T. H. M. Housmans; V. Rosca; M. T. M. Koper, *J. Appl. Electrochem.* **2006**, *36*, 1215-1221.
[13] P. Abril; M. P. del Río; C. Tejel; T. W. G. M. Verhoeven; J. W. H. Niemantsverdriet; C. J. M. van der Ham; K. G. Kottrup; D. G. H. Hetterscheid, *ACS Catal.* **2016**, *6*, 7872-7875.

[14] U. Hintermair; S. W. Sheehan; A. R. Parent; D. H. Ess; D. T. Richens; P. H. Vaccaro; G. W. Brudvig; R. H. Crabtree, *J. Am. Chem. Soc.* **2013**, *135*, 10837-10851.
[15] B. Limburg; E. Bouwman; S. Bonnet, *Coord. Chem. Rev.* **2012**, *256*, 1451-1467.
[16] O. Diaz-Morales; F. Calle-Vallejo; C. de Munck; M. T. M. Koper, *Chem. Sci.* **2013**, *4*, 2334-2343.
[17] G. Chen; L. Chen; S. M. Ng; W. L. Man; T. C. Lau, *Angew. Chem., Int. Ed.* **2013**, *52*, 1789-1791.
[18] Y. Lin; S. Zhou; S. W. Sheehan; D. Wang, *J. Am. Chem. Soc.* **2011**, *133*, 2398-2401.
[19] M. T. Mayer; C. Du; D. Wang, *J. Am. Chem. Soc.* **2012**, *134*, 12406-12409.
[20] K. M. H. Young; B. M. Klahr; O. Zandi; T. W. Hamann, *Catal. Sci. Technol.* **2013**, *3*, 1660-1671.
[21] N. D. Schley; J. D. Blakemore; N. K. Subbaiyan; C. D. Incarvito; F. D'Souza; R. H. Crabtree; G. W. Brudvig, *J. Am. Chem. Soc.* **2011**, *133*, 10473-10481.
[22] C. J. M. van der Ham; F. Işık; T. W. G. M. Verhoeven; J. W. Niemantsverdriet; D. G. H. Hetterscheid, *Catal. Today* **2017**, *290*, 33-38.
[23] J. Björk; F. Hanke; C.-A. Palma; P. Samori; M. Cecchini; M. Persson, *J. Phys. Chem. Lett.* **2010**, *1*, 3407-3412.
[24] A. Rochefort; J. D. Wuest, *Langmuir* **2009**, *25*, 210-215.
[25] S. D. Chakarova-Kack; E. Schroder; B. I. Lundqvist; D. C. Langreth, *Phys. Rev. Lett.* **2006**, *96*, 146107.
[26] M. A. Morales Vásquez; M. Hamer; N. I. Neuman; A. Y. Tesio; A. Hunt; H. Bogo; E. J. Calvo; F. Doctorovich, *ChemCatChem* **2017**.
[27] C. Rajesh; C. Majumder; H. Mizuseki; Y. Kawazoe, *J. Chem. Phys.* **2009**, *130*, 124911.
[28] Z. Wang; H. Lei; R. Cao; M. Zhang, *Electrochim. Acta* **2015**, *171*, 81-88.
[29] J. M. Saveant; E. Vianello, *Electrochim. Acta* **1965**, *10*, 905-920.
[30] J. L. Fillol; Z. Codola; I. Garcia-Bosch; L. Gomez; J. J. Pla; M. Costas, *Nat. Chem.* **2011**, *3*, 807-813.
[31] B. Das; B. L. Lee; E. A. Karlsson; T. Akermark; A. Shatskiy; S. Demeshko; R. Z. Liao; T. M. Laine; M. Haukka; E. Zeglio; A. F. Abdel-Magied; P. E. Siegbahn; F. Meyer; M. D. Karkas; E. V. Johnston; E. Nordlander; B. Akermark, *Dalton Trans.* **2016**, *45*, 13289-13293.
[32] W. C. Ellis; N. D. McDaniel; S. Bernhard; T. J. Collins, *J. Am. Chem. Soc.* **2010**, *132*, 10990-10991.
[33] T. Norrby; A. Börje; L. Zhang; B. Åkermark; J. H. Wagenknecht; G. W. Francis; J. Szúnyog; B. Långström, *Acta Chem. Scand.* **1998**, *52*, 77-85.
[34] J. Yin; B. Xiang; M. A. Huffman; C. E. Raab; I. W. Davies, *J. Org. Chem.* **2007**, *72*, 4554-4557.
[35] S. Zheng; N. R. Reintjens; M. A. Siegler; O. Roubeau; E. Bouwman; A. Rudavskyi; R. W. Havenith; S. Bonnet, *Chem. - Eur. J.* **2016**, *22*, 331-339.